

Simultaneous multitone microwave emission by DC-driven spintronic nano-element

A. Hamadeh,¹ D. Slobodianiuk,^{2,3} R. Moukhader,⁴ G. Melkov,² V. Borynskiy,³ M. Mohseni,¹ G. Finocchio,⁴ V. Lomakin,⁵ R. Verba,³ G. de Loubens,⁶ P. Pirro,¹ and O. Klein⁷

¹*Fachbereich Physik and Landesforschungszentrum OPTIMAS, Technische Universität Kaiserslautern, 67663 Kaiserslautern, Germany*

²*Taras Shevchenko National University of Kyiv, Kyiv 01601, Ukraine*

³*Institute of Magnetism, Kyiv 03142, Ukraine*

⁴*Dept. Mathematical and Computer Sciences, Physical Sciences and Earth Sciences, University of Messina, 98166 Messina, Italy*

⁵*Center for Magnetic Recording Research, University of California San Diego, La Jolla, California 92093-0401, USA*

⁶*SPEC, CEA, CNRS, Université Paris-Saclay, 91191 Gif-sur-Yvette, France*

⁷*Univ. Grenoble Alpes, CEA, CNRS, Grenoble INP, INAC-Spintec, 38054 Grenoble, France*

(Dated: October 19, 2022)

Current-induced self-sustained magnetization oscillations in spin-torque nano-oscillators (STNOs) are promising candidates for ultra-agile microwave sources or detectors. While usually STNOs behave as a monochrome source, we report here clear bimodal simultaneous emission of incommensurate microwave oscillations, where the two tones correspond to two parametrically coupled eigenmodes with tunable splitting. The emission range is crucially sensitive to the change in hybridization of the eigenmodes of free and fixed layers, for instance, through a slight tilt of the applied magnetic field from the normal of the nano-pillar. Our experimental findings are supported both analytically and by micromagnetic simulations, which ascribe the process to four-magnon scattering between a pair of radially symmetric magnon modes and a pair of magnon modes with opposite azimuthal index. Our findings open up new possibilities for cognitive telecommunications and neuromorphic systems that use frequency multiplexing to improve communication performance.

A great number of research projects has been devoted to the study of spin transfer torque (STT) after its theoretical prediction [1, 2]. This new paradigm is meant to ignite a conceptual metamorphosis of spintronics, a research field which capitalizes on the spin degree of freedom of the electron [3]. The STT effect can enable a variety of spintronics applications, such as spin-torque magnetic random access memories (MRAM) [4] and spin-torque nano-oscillators (STNOs) [5]. The use of STNOs to generate microwave signals in nanoscale devices has generated tremendous and continuous research interest in recent years [6–10]. Their key features are frequency tunability [11], nanoscale size [10], broad working temperature [12], and easy integration with the standard silicon technology [6, 13]. As strongly nonlinear devices, STNOs can exhibit different dynamic regimes, which are promising candidates for various applications including microwave signal generation and detection [14–16], signal modulation [17], spin wave generation [18], neuromorphic computing [19–21], etc.

Generally, only a *single* mode is expected to oscillate at one time in an STNO as predicted by the universal oscillator model [22]. Multimodal co-generation of weak commensurate tones can be produced by harmonic distortion. Here, the tones are intrinsically linked by rational numbers. Alternatively, mode hopping between nearly degenerate eigen-solutions have been reported [23–25] induced by thermal fluctuations [26], spatial inhomogeneity of the internal field in asymmetric ferromagnetic bilayers [27], or by formation of higher-order modes of excited magnetic solitons [28]. Also, high level of thermal

fluctuations can result in a seemingly multimode generation that, in fact, is just an amplification of incoherent thermal population of higher modes.

In this letter, we find and elucidate another possibility to create stable *simultaneous* excitation of multi spin-wave modes in an STO with a continuously adjustable splitting. The leading order mechanism supporting multimode generation is found to be four-magnon scattering or, in other words, second-order parametric instability. Although this process is well-known in magnetic systems [29–32], its observation in an STNO is often prohibited as it is impossible to satisfy both energy and angular momentum conservation rules. We found parametric instability becomes possible because of strong hybridization between the modes of the two layers of the STNO, which also makes the parametric process highly sensitive to external conditions and thus controllable.

The studied STNO is a circular nanopillar with diameter of 250 nm consisting of (Cu60|Py15|Cu10|Py4|Au25) layers (numbers indicate the thickness in nanometers), fabricated by electron beam lithography, in which top and bottom Au and Cu electrodes were designed for microwave transport measurements. The STNO is excited by a negative dc current I_{dc} , corresponding to an electron flow from the thin to the thick magnetic layer, which allows us to observe STT-induced microwave generation. In the measurements presented below, a bias magnetic field in the range $H_{ext} = (8.5 - 9.6)$ kOe was applied at $\theta_H = 2^\circ$ from the sample normal (see Fig. 1(a)). This tilt is introduced in order to create a small misalignment between the static magnetizations of the layers, which is

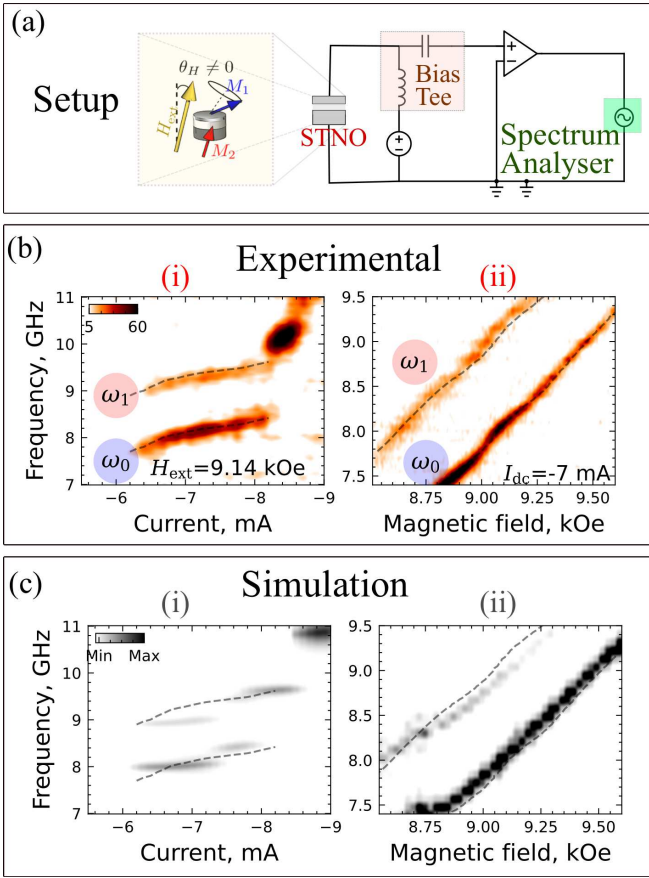


FIG. 1. (a) Experimental setup for electrical measurement. A dc current is passed through the STNO, while the ac component is extracted via a bias-tee and measured with a spectrum analyzer. (b,d) Dependence of the microwave generation characteristics of the STNO on the dc current at constant bias field $H_{ext} = 9.14$ kOe (b, d), and (c,e) on the external field at a fixed dc current $I = -7$ mA; (b,c) - experiment, (d,e) - micromagnetic simulations showing the oscillations of two modes simultaneously. Dashed lines show the location of the oscillation modes in the experiment and the intensity scale indicates the normalized power (in fW/GHz for the experimental data).

required for the appearance of resistance (and voltage) oscillations under almost circular magnetization precession; in the case of $\theta_H = 0^\circ$ voltage oscillations vanish [33]. However, this symmetry breaking also has significant consequences on the entire dynamics, as discussed in the following.

First, the bias current dependence of the voltage oscillation spectra under a constant magnetic field $H_{ext} = 9.14$ kOe is reported in Fig. 1(b). Within the current range from -6 mA to -8 mA, we observe two simultaneously auto-oscillating modes [34], referred below as ω_0 and ω_1 , which are split by about 1.1 GHz. With a further current increase, the generation frequency exhibits a pronounced jump and generation becomes seemingly single-mode (the second mode is hardly detectable). Also, this

jump is accompanied by a substantial power increase (see intensity scale and supplementary materials [35]). At even higher currents, the STNO generation demonstrates further frequency jumps and complex dynamics that are not considered here. Within the bimodal regime at $I_{dc} = (-6, -8.2)$ mA, the frequencies of both modes demonstrate the same weak increase with the current amplitude, which is unexpected for almost perpendicularly magnetized STO, characterized by a strong nonlinear frequency shift [22].

Fig. 1(c) presents the frequency evolution with the strength of a magnetic field under a constant dc current $I_{dc} = -7$ mA. The bimodal regime is robust to the field strength variation and is observed in the entire presented field range. The frequencies of both oscillation modes ω_0 and ω_1 vary almost linearly with the applied field; in almost perpendicularly magnetized STNO such dependence is not trivial as it may appear, indicating a significant nonlinear damping effect [22]. It is worth noting that in the case of perpendicular magnetization ($\theta_H = 0^\circ$), the generation characteristics of the STNO become fairly standard and none of the features described here indicating bimodal generation were observed [33, 35].

To get a deeper insight into the magnetization dynamics, micromagnetic simulations were performed using the FastMag software package [36] that is based on the finite elements method (FEM). FastMag allows computing the full system including interactions between the reference and free layer via mutual spin transfer torque effects. FastMag also calculates the magneto-resistance response that can be directly compared to the experimental measurements. Material parameters were taken from the experimental study of passive dynamics (i.e., below auto-oscillation threshold) of the nanopillar [37] (see details in supplementary [35]). The FEM mesh edge length was chosen as 4 nm. The data evaluation of simulation was done through Aithericon [38].

To excite the oscillation dynamics, a negative dc current was applied through the structure. The results of these micromagnetic simulations, shown in Fig. 1(d-e), reproduce the experimental measurements with a good qualitative and quantitative agreement, a clear indication that the advanced micromagnetic modeling is able to capture the features leading to the observed complex behavior. Reference simulations performed for the case $\theta_H = 0^\circ$ show standard single-mode STNO behavior, in accordance with previous experimental study [33].

Next, we investigate spectra of the magnetization dynamics by evaluating the fast Fourier transform (FFT) of the circularly polarized transverse magnetization components $M_+ = M_x + iM_y$ emitted by the electrically driven STNO, where i is the imaginary unit. In contrast to the resistance oscillation spectra, they demonstrate *three* peaks – an additional peak, referred to as ω_2 , is visible below ω_0 (Fig. 2). The frequency of the peaks satisfies the relation $2\omega_0 = \omega_1 + \omega_2$, which leads us to the assump-

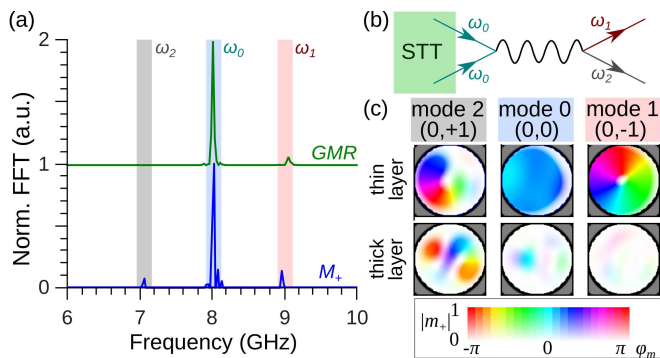


FIG. 2. (a) Frequency spectrum of the M_+ magnetization component (blue line) and spectrum of the magnetoresistance oscillations (green line, vertically offset) of the STNO under a bias current $I_{dc} = -7$ mA, obtained by micromagnetic simulations. (b) A diagram illustrating the four-magnon scattering process leading to the multimode generation in the STNO. (c) Spatially resolved magnetization precession patterns of the three modes, obtained via FFT of magnetization time traces. The brightness indicates the amplitude and the hue indicates the phase.

tion that four-magnon interaction between these modes, schematically shown in Fig. 2(b), is involved in STNO dynamics. Using a mesh resolved FFT, we obtain the spatial profiles of the excitations corresponding to these peaks. The main mode ω_0 is a quasi-uniform mode characterized by respectively a radial index $m = 0$ and an azimuthal index $\ell = 0$, which we label $(m = 0, \ell = 0)$ mode. This mode can be identified as the lowest-frequency mode of the isolated free layer. The peak at ω_1 is the $(0, -1)$ azimuthal mode, also mostly localized within the free layer. The excitation at ω_2 resembles the $(0, +1)$ azimuthal mode. However, in contrast to other excitations, this mode has comparable oscillation amplitude in *both* thin and thick STNO layers indicating a strong hybridization.

To elucidate the nature of the signal at ω_2 , we performed micromagnetic simulations of the STNO modes in the passive regime (no dc current) [35]. We found that in our device, the $\ell = \pm 1$ azimuthal eigenmodes of the thick layer are located below the fundamental mode of the thin layer (because of different saturation magnetization, see supplement) and these modes experience strong hybridization so that the oscillation amplitude is comparable in both layers (Fig. 3(b)). The last fact explains why the mode at ω_2 is not visible in GMR spectra: the relative angle between the layers magnetizations is only weakly changed when it is excited. Thus, we attribute the multimode generation to a four-magnon process involving the fundamental mode $(0,0)$ of the thin layer, the azimuthal $(0, -1)$ mode of the thin layer and the $(0, +1)$ mode of the thick layer that is strongly hybridized to the thin layer. This process satisfies the momentum conservation rule $2\ell_0 = \ell_1 + \ell_2$ and the mode

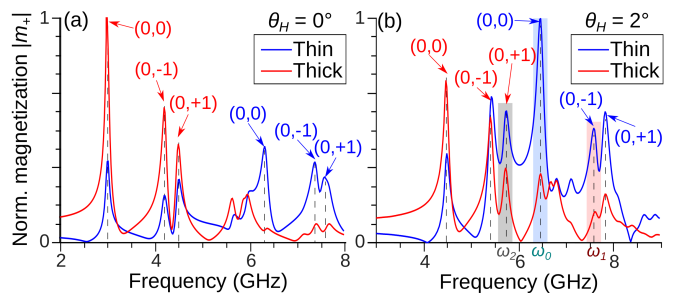


FIG. 3. Spectra of linear (low-amplitude) magnetization oscillations of the STNO nanopillar, excited by spatially nonuniform magnetic field (micromagnetic simulations); the modulus of averaged in a quarter of thin and thick layers dynamic magnetization \mathbf{m}_+ , normalized to maximal value, is shown.

eigenfrequencies are reasonably close to the energy conservation rule $2\omega_0 = \omega_1 + \omega_2$. An additional check that the thick layer mode is involved in the multimode generation was made by simulating the active STNO with a drastically increased local field in the thick layer. In this case, the thick layer modes are shifted to much higher frequencies and the above-mentioned four-magnon process becomes impossible. Indeed, no multimode generation was observed in this case. In the reference case of a perpendicular field, the thick layer modes shift to lower frequencies and thus experience much less hybridization (Fig. 3(a)), which is crucial for the multimode generation as discussed below.

In the following, we consider an analytical model to describe the dynamics of STNO modes including parametric coupling. As before, we denote the fundamental mode as mode “0” having the amplitude a_0 , the $(0, -1)$ mode of the thin layer and $(0, +1)$ thick layer mode as modes 1 and 2, respectively, and consider dynamics of only these three modes. The mentioned four-magnon process is described by the term $\mathcal{H}^{(4)} = W_{00,12}a_1a_2a_0^* + \text{c.c.}$ in the Hamiltonian of the system. Taking it into account, the dynamics of the coupled modes is described by equations

$$\begin{aligned} \dot{a}_0 + i\tilde{\omega}_0a_0 + \tilde{\Gamma}_0a_0 &= -2iW_{00,12}a_1^*a_2, \\ \dot{a}_1 + i\tilde{\omega}_1a_1 + \tilde{\Gamma}_1a_1 &= -iW_{00,12}^*a_0^2a_2^*, \\ \dot{a}_2 + i\tilde{\omega}_2a_2 + \tilde{\Gamma}_2a_2 &= -iW_{00,12}^*a_0^2a_1^*. \end{aligned} \quad (1)$$

Here, an overdot denotes time derivative, $\dot{a} = \partial_t a$, $\tilde{\omega}_i$ and $\tilde{\Gamma}_i$ are frequency and total damping of i -th mode accounting for nonlinear contributions. In a general case, “total” frequency includes linear eigenfrequency, self and cross-nonlinear shifts from all modes: $\tilde{\omega}_i = \omega_i + T_i|a_i|^2 + 2\sum_{j \neq i} T_{ij}|a_j|^2$. The total damping accounts for nonlinear changes of both the damping and the STT anti-damping torque [22]: $\tilde{\Gamma}_i = \Gamma_i(1 + \xi_i|a_i|^2 + 2\sum_{j \neq i} \xi_{ij}|a_j|^2) - \sigma_i I(1 - \tilde{\xi}_i|a_i|^2 - 2\sum_{j \neq i} \tilde{\xi}_{ij}|a_j|^2)$, where $\Gamma_i = \alpha_G \omega_i$ is the linear Gilbert damping and σ is the STT efficiency and $\tilde{\xi}_{ij}$ is the nonlinear coefficients (see supplement).

Since the energy of mode 2 is more concentrated in the thick layer, while modes 0 and 1 are concentrated in the thin one, we neglect all related frequency and damping cross shifts, such as $T_{i2} = 0$, $\xi_{i2} = 0$, etc. Only for STT term ($\tilde{\xi}_{2i}$), such simplification is not appropriate since it is inversely proportional to the layer thickness, so the thin layer contribution to the total STT could be dominant even for mode 2. Linear frequencies for the model were extracted from micromagnetic data and nonlinear coefficients were estimated using the vector Hamiltonian formalism [39, 40], as described in Supplementary materials [35].

When the current increases, mode 0 first turns to the self-oscillation regime; this happens at $I_{\text{th}} = \Gamma_0/\sigma$ (corresponding to -6 mA in the experiment). Formal thresholds of “isolated” modes 1 and 2 Γ_i/σ_i are larger, but competition for common STT pumping prohibits excitation of higher-order modes above their formal thresholds in the absence of other coupling [26], and the only source for their excitation is the parametric instability of the mode 0. Then, assuming negligible amplitudes of the modes 1 and 2, we can calculate the “virtual” amplitude of mode 0 above the threshold in the absence of other modes, $|a_0|^2 = (\sigma I - \Gamma_0)/(\xi_0(\sigma I - \Gamma_0))$ [22], and the threshold amplitude a_{th} of mode 0, above which parametric instability develops, [40]

$$|a_{\text{th}}|^2 = \frac{\sqrt{\tilde{\Gamma}_1 \tilde{\Gamma}_2}}{|W_{00,12}|} \sqrt{1 + \frac{(2\tilde{\omega}_0 - \tilde{\omega}_1 - \tilde{\omega}_2)^2}{(\tilde{\Gamma}_1 + \tilde{\Gamma}_2)^2}}. \quad (2)$$

Here, the nonlinear frequency and the damping are calculated for the free-running amplitude of mode 0 at a given current and vanishing amplitudes of other modes. If $|a_0| > |a_{\text{th}}|$, then the parametric instability occurs and modes 1 and 2 are excited.

Dependencies of the isolated free-running amplitude a_0 and the parametric instability threshold are shown in Fig. 4(a,b). In the case of $\theta_H = 2^\circ$, the threshold is overcome in a certain range of currents, and a three-mode generation is expected. In contrast, in the reference case of a perpendicular field, the instability threshold is never overcome, and single-mode generation is expected. There are two reasons for this difference. The first one is the larger detuning from exact parametric resonance $\Delta\omega = 2\tilde{\omega}_0 - \tilde{\omega}_1 - \tilde{\omega}_2$ (see Fig. 4(a,b)) because of the different positions of the thick layer eigenmodes. However, this difference is not drastic and the second reason, namely the significantly (threefold) reduced parametric coupling $W_{00,12}$ also plays a crucial role. The latter is a result of the much lower hybridization of the modes, which is clear from the comparison of the oscillation amplitude in the thin layer at the position of (0, +1) mode of the thick layer in Fig. 3 (see calculation details in supplementary materials [35]). The same reason determines the explanation for the observation of this particular pair of parametric modes at $\theta_H = 2^\circ$. Another pair, which also satisfies the

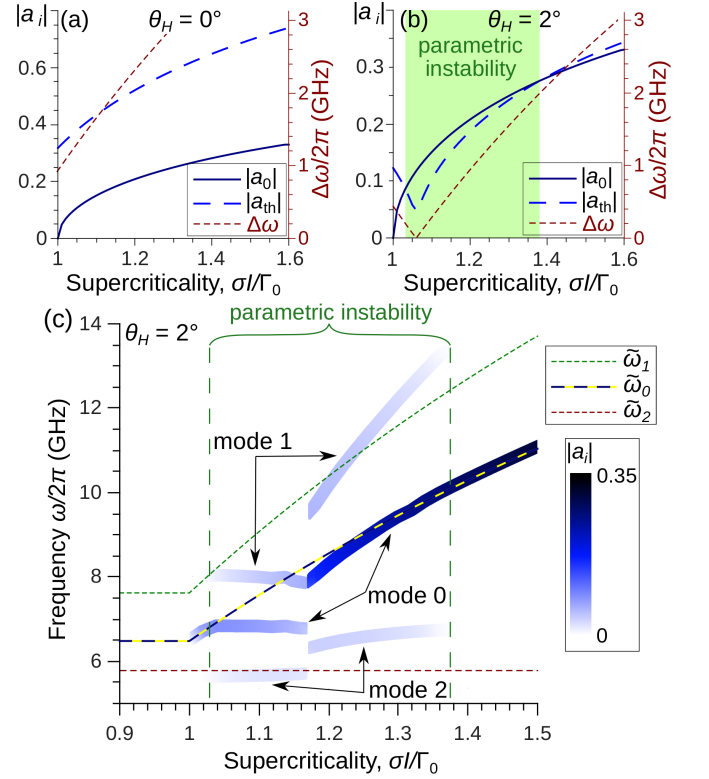


FIG. 4. (a,b) Free-running amplitude a_0 of the mode 0 in the absence of parametric coupling, threshold of the parametric instability a_{th} (both - left axis), and detuning from parametric resonance condition $\Delta\omega$ (right axis) in the case of perpendicular (a) and tilted (b) field. (c) Current dependence of stationary frequency and amplitude (color-coded) of the interacting modes, obtained as numerical integration of model Eq. (1) for $\theta_H = 2^\circ$; dashed lines show free-running frequency $\tilde{\omega}_0$ and eigenfrequencies $\tilde{\omega}_1, \tilde{\omega}_2$ which would be observed without parametric coupling.

momentum conservation ((0, -1) thick layer mode and (0, +1) thin layer mode), exhibits smaller parametric coupling because of lower hybridization of the (0, -1) thick layer mode (Fig. 3(b)).

Finally, we numerically integrate Eqs. 1 and present the stationary mode frequencies and amplitudes in Fig. 4(c). Starting from the threshold $\sigma I = \Gamma_0$, the amplitude and frequency of the mode 0 increase and reach the parametric instability threshold ($\sigma I/\Gamma_0 \approx 1.035$). Above this instability threshold, all three modes are excited and their frequencies are almost frozen (a feature that could be interesting for certain applications). In this regime, the parametric process dominates and the modes have stationary amplitudes that almost satisfy the parametric resonance condition $2\tilde{\omega}_0(a_i) \approx \tilde{\omega}_1(a_i) + \tilde{\omega}_2(a_i)$. Above $\sigma I/\Gamma_0 \approx 1.18$ this generation regime cannot be sustained anymore, and we observed an abrupt jump of the mode frequencies and amplitudes as discerned in the experiment (see Fig. 1(b)). Mode 0 acquires an amplitude and a frequency that are close to the ones in the absence

of parametric pumping, while modes 1 and 2 oscillate far from their “nonlinear eigenfrequencies” (i.e., the parametric process becomes strongly nonresonant). Their amplitudes decrease up to the current $\sigma I/\Gamma_0 \approx 1.36$, above which the instability threshold becomes too high and the STNO returns to single-mode regime. Within the multimode generation range, the amplitude of parametric mode 1 is evidently larger than of the mode 2. This can be attributed to the substantially larger total damping rate of the mode 2. This circumstance also complicates the experimental observation of mode 2.

Overall, the model results are very similar to experimental observations. The finite range of multimode generation, the small (vanishing) frequency slope, the almost constant oscillation amplitude in the multimode regime, and the frequency jump are all observed in experiment. There is a quantitative difference in mode oscillation frequencies, which is on account of (i) the approximate calculation of nonlinear coefficients, particularly the phenomenological coefficient of nonlinear damping, and (ii) neglecting of the Oersted fields in the model that, according to experimental measurements below the threshold, result in the mode frequency increase about 70 MHz/mA, almost the same for different modes.

To conclude, we found by experiment a regime of simultaneous multimode microwave emission by a nanopillar-based STO. The physical process behind this is a second-order parametric instability between a pair of radially symmetric magnon modes and a pair of opposite azimuthal index modes, without any spatio-temporal overlap. The process, however, satisfies the constraint of both angular momentum and energy conservation through the hybridization of eigenmodes between the thin and the thick layer. This co-generation has the additional feature of being incommensurable. The splitting between modes can thus be tuned by changing the characteristics of the nano-pillar such as its diameter. A future work direction will be to exploit non-uniform magnetic textures as a means to control continuously the splitting by an external bias parameter, such as the magnetic field. A particularly promising candidate is the vortex, where the splitting between the $\ell = \pm 1$ has been shown to vary strongly as a function of H_0 . We believe that the simultaneous self-generation of multiple frequencies in dc-driven spintronic elements has large potential for applications using frequency multiplexing techniques in neuromorphic and wave-based approaches.

This work has been supported by the European Research Council within the Starting Grant No. 101042439 “CoSpiN” and by the Deutsche Forschungsgemeinschaft (DFG, German Research Foundation) - TRR 173 - 268565370 (project B01) and by the French Grants ANR-21-CE24-0031 Harmony and the EU-project H2020-2020-FETOPEN k-NET-899646 and by the National Academy of Sciences of Ukraine, project #0122U002462 and the project PRIN 2020LWPKH7

funded by the Italian Ministry of University and Research.

-
- [1] J. C. Slonczewski, *J. Magn. Magn. Mater.* **159**, L1 (1996).
 - [2] L. Berger, *Phys. Rev. B* **54**, 9353 (1996).
 - [3] S. Wolf, D. Awschalom, R. Buhrman, J. Daughton, v. S. von Molnár, M. Roukes, A. Y. Chtchelkanova, and D. Treger, *science* **294**, 1488 (2001).
 - [4] L. Thomas, G. Jan, J. Zhu, H. Liu, Y.-J. Lee, S. Le, R.-Y. Tong, K. Pi, Y.-J. Wang, D. Shen, *et al.*, *J. Appl. Phys.* **115**, 172615 (2014).
 - [5] A. Hirohata, K. Yamada, Y. Nakatani, I.-L. Prejbeanu, B. Diény, P. Pirro, and B. Hillebrands, *J. Magn. Magn. Mater.* **509**, 166711 (2020).
 - [6] S. I. Kiselev, J. C. Sankey, I. N. Krivorotov, N. C. Emley, R. J. Schoelkopf, R. A. Buhrman, and D. C. Ralph, *Nature* **425**, 380 (2003).
 - [7] Q. Mistral, J.-V. Kim, T. Devolder, P. Crozat, C. Chappert, J. A. Katine, M. J. Carey, and K. Ito, *Appl. Phys. Lett.* **88**, 192507 (2006).
 - [8] D. Houssameddine, S. Florez, J. Katine, J.-P. Michel, U. Ebels, D. Mauri, O. Ozatay, B. Delaet, B. Viala, L. Folks, *et al.*, *Appl. Phys. Lett.* **93**, 022505 (2008).
 - [9] Q. Mistral, M. van Kampen, G. Hrkac, J.-V. Kim, T. Devolder, P. Crozat, C. Chappert, L. Lagae, and T. Schrefl, *Phys. Rev. Lett.* **100**, 257201 (2008).
 - [10] Z. Zeng, G. Finocchio, and H. Jiang, *Nanoscale* **5**, 2219 (2013).
 - [11] S. Bonetti, P. Muduli, F. Mancoff, and J. Åkerman, *Appl. Phys. Lett.* **94**, 102507 (2009).
 - [12] O. V. Prokopenko, E. Bankowski, T. Meitzler, V. S. Tiberkevich, and A. N. Slavin, *IEEE Trans. Magn.* **48**, 3807 (2012).
 - [13] W. H. Rippard, M. R. Pufall, S. Kaka, S. E. Russek, and T. J. Silva, *Phys. Rev. Lett.* **92**, 027201 (2004).
 - [14] E. Grimaldi, R. Lebrun, A. Jenkins, A. Dussaux, J. Grollier, V. Cros, A. Fert, H. Kubota, K. Yakushiji, A. Fukushima, *et al.*, in *2014 IEEE International Frequency Control Symposium (FCS)* (IEEE, 2014) pp. 1–6.
 - [15] S. Louis, V. Tyberkevych, J. Li, I. Lisenkov, R. Khymyn, E. Bankowski, T. Meitzler, I. Krivorotov, and A. Slavin, *IEEE Trans. Magn.* **53**, 1 (2017).
 - [16] A. Litvinenko, V. Iurchuk, P. Sethi, S. Louis, V. Tyberkevych, J. Li, A. Jenkins, R. Ferreira, B. Dieny, A. Slavin, *et al.*, *Nano Lett.* **20**, 6104 (2020).
 - [17] W. Skowroński, J. Chęciński, S. Ziętek, K. Yakushiji, and S. Yuasa, *Sci. Rep.* **9**, 1 (2019).
 - [18] M. Madami, S. Bonetti, G. Consolo, S. Tacchi, G. Carlotto, G. Gubbiotti, F. Mancoff, M. A. Yar, and J. Åkerman, *Nature nanotechnology* **6**, 635 (2011).
 - [19] J. Torrejon, M. Riou, F. A. Araujo, S. Tsunegi, G. Khalsa, D. Querlioz, P. Bortolotti, V. Cros, K. Yakushiji, A. Fukushima, *et al.*, *Nature* **547**, 428 (2017).
 - [20] J. Grollier, D. Querlioz, and M. D. Stiles, *Proceedings of the IEEE* **104**, 2024 (2016).
 - [21] M. Riou, J. Torrejon, B. Garitain, F. A. Araujo, P. Bortolotti, V. Cros, S. Tsunegi, K. Yakushiji, A. Fukushima, H. Kubota, *et al.*, *Phys. Rev. Applied* **12**, 024049 (2019).
 - [22] A. Slavin and V. Tiberkevich, *IEEE Trans. Magn.* **45**,

- 1875 (2009).
- [23] A. Eklund, S. Sani, S. Mohseni, J. Persson, B. Malm, and J. Åkerman, in *Noise and Fluctuations (ICNF), 2013 22nd International Conference on* (doi=10.1109/ICNF.2013.6578965, 2013) pp. 1–4.
- [24] O. Heinonen, P. Muduli, E. Iacocca, and J. Åkerman, *IEEE Trans. Magn.* **49**, 4398 (2013).
- [25] E. Iacocca, O. Heinonen, P. K. Muduli, and J. Åkerman, *Phys. Rev. B* **89**, 054402 (2014).
- [26] D. V. Slobodianiuk, *Cond. Matter Phys.* **17**, 13801 (2014).
- [27] L. Chen, W. Wang, X. Zhan, K. Zhou, Z. Gao, L. Liang, T. Zhou, Y. Du, and R. Liu, *Phys. Rev. B* **105**, 104413 (2022).
- [28] L. Yang, R. Verba, V. Tiberkevich, T. Schneider, A. Smith, Z. Duan, B. Youngblood, K. Lenz, J. Lindner, A. N. Slavin, and I. N. Krivorotov, *Sci. Rep.* **5**, 16942 (2015).
- [29] V. S. L'vov, *Wave Turbulence under Parametric Excitation* (Springer-Verlag, New York, 1994).
- [30] H. Suhl, *Journal of Physics and Chemistry of Solids* **1**, 209 (1957).
- [31] P. Pirro, V. I. Vasyuchka, A. A. Serga, and B. Hillebrands, *Nature Reviews Materials* **6**, 1114–1135 (2021).
- [32] P. Pirro, T. Sebastian, T. Brächer, A. A. Serga, T. Kubota, H. Naganuma, M. Oogane, Y. Ando, and B. Hillebrands, *Physical Review Letters* **113**, 227601 (2014).
- [33] A. Hamadeh, G. De Loubens, V. Naletov, J. Grollier, C. Ulysse, V. Cros, and O. Klein, *Phys. Rev. B* **85**, 140408 (2012).
- [34] We have checked it experimentally by performing a synchronization experiment. It showed that both ω_0 and ω_1 are locked together when an external oscillation is additionally applied at either ω_0 or ω_1 . We interpret this as a proof of the simultaneity of the emission.
- [35] Supplementary materials are located at ... They contain: (i) description of micromagnetic simulations, (ii) current dependence of generation power for perpendicular and tilted fields, and (iii) details of the parameters calculations for theoretical model.
- [36] R. Chang, S. Li, M. Lubarda, B. Livshitz, and V. Lomakin, *J. Appl. Phys.* **110**, 039907 (2011).
- [37] V. V. Naletov, G. De Loubens, G. Albuquerque, S. Borlenghi, V. Cros, G. Faini, J. Grollier, H. Hurdequint, N. Locatelli, B. Pigeau, *et al.*, *Phys. Rev. B* **84**, 224423 (2011).
- [38] www.aithericon.com.
- [39] V. Tyberkevych, A. Slavin, P. Artemchuk, and G. Rowlands, “[Vector Hamiltonian Formalism for Nonlinear Magnetization Dynamics](#),” (2020), arXiv:2011.13562 [cond-mat.mtrl-sci].
- [40] R. Verba, L. Körber, K. Schultheiss, H. Schultheiss, V. Tiberkevich, and A. Slavin, *Phys. Rev. B* **103**, 014413 (2021).

Simultaneous multitone microwave emission by DC-driven spintronic nano-element

A. Hamadeh,¹ D. Slobodianiuk,^{2,3} R. Moukhader,⁴ G. Melkov,² V. Borynskiy,³ M. Mohseni,¹ G. Finocchio,⁴ V. Lomakin,⁵ R. Verba,³ G. de Loubens,⁶ P. Pirro,¹ and O. Klein⁷

¹Fachbereich Physik and Landesforschungszentrum OPTIMAS, Technische Universität Kaiserslautern, 67663 Kaiserslautern, Germany

²Taras Shevchenko National University of Kyiv, Kyiv 01601, Ukraine

³Institute of Magnetism, Kyiv 03142, Ukraine

⁴Dept. Mathematical and Computer Sciences, Physical Sciences and Earth Sciences, University of Messina, 98166 Messina, Italy

⁵Center for Magnetic Recording Research, University of California San Diego, La Jolla, California 92093-0401, USA

⁶SPEC, CEA, CNRS, Université Paris-Saclay, 91191 Gif-sur-Yvette, France

⁷Univ. Grenoble Alpes, CEA, CNRS, Grenoble INP, INAC-Spintec, 38054 Grenoble, France

I. GENERATION POWER DEPENDENCE

Figure S1 shows experimental measurements of integrated generation power of the STNO at different applied field angle, $\theta_H = 2^\circ$ and $\theta_H = 0^\circ$. The generation power is measured by the method of magnetic resonance force microscopy, as described in [1]. For almost perpendicular static magnetization and close to circular magnetization precession, the change in the longitudinal magnetization component ΔM_z is linearly proportional to integrated oscillations power. For $\theta_H = 0^\circ$ the current dependence of the power is standard without any peculiarities. In contrast, at $\theta_H = 2^\circ$, the power dependence demonstrates a plateau around -7 mA and an abrupt increase near the current value of -8.2 mA, where generation frequency experiences a jump, as discussed in the main text (Fig. 1(b) in the main text).

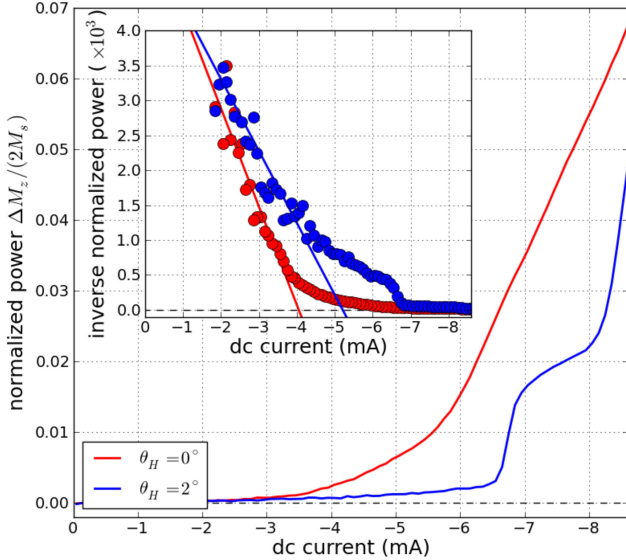


FIG. S1. Normalized integrated power of STNO generation at different angle of the bias field. Inset – inverse power dependence, showing slightly different auto-oscillation thresholds for the considered cases.

II. MICROMAGNETIC SIMULATIONS

In all the micromagnetic simulations we use the following material parameters, which were experimentally determined from the passive STNO dynamics [2]: saturation magnetization of the thin layer $\mu_0 M_{s,\text{thin}} = 0.82$ T and of the thick layer $\mu_0 M_{s,\text{thick}} = 0.96$ T; Gilbert damping parameter $\alpha_{G,\text{thin}} = 0.015$ and $\alpha_{G,\text{thick}} = 0.0085$, respectively, gyromagnetic ratio $\gamma = 1.87 \times 10^{11} \text{ s}^{-1} \text{ T}^{-1}$ and exchange stiffness $A = 10.5 \text{ pJ/m}$ are identical in both layers; spin-polarization efficiency $\epsilon = 0.3$ [1]. In the simulations of active STNO dynamics, we account for mutual spin-transfer torque in both layers and effect of Oersted fields.

Simulations of linear spin-wave eigenmodes, presented in Fig. 3 in the main text, were performed at zero dc current and, consequently, zero Oersted fields. Microwave magnetic field $\mathbf{b} = b_{rf} \mathbf{e}_y$ was applied in one quarter of the pillar, and dynamic magnetization was also recorded in a quarter, so that azimuthal modes $\ell = \pm 1, \pm 2$, (except for the modes with azimuthal numbers $m = \pm 4, \pm 8, \dots$) become visible.

III. CALCULATION OF PARAMETERS FOR ANALYTICAL MODEL

Linear frequencies for the model Eq. (1) were extracted from micromagnetic data. They are equal to $\omega_0/2\pi = 6.32$ GHz, $\omega_1/2\pi = 7.36$ GHz, $\omega_2/2\pi = 4.48$ GHz for the case of perpendicular field, and $\omega_0/2\pi = 6.48$ GHz, $\omega_1/2\pi = 7.62$ GHz, $\omega_2/2\pi = 5.78$ GHz for $\theta_H = 2^\circ$.

Calculation of nonlinear parameters is a complex task. For spin-wave eigenmodes in magnetic nanostructures it can be solved by using the recently developed vector Hamiltonian formalism for SW dynamics [3] and micromagnetically simulated mode profiles. Within this formalism, the four-magnon part of the Hamiltonian is given by

$$\mathcal{H}^{(4)} = \int \frac{\omega_M}{8V} \left(|s|^2 \boldsymbol{\mu}_0 \cdot \hat{\mathbf{N}} \cdot (|s|^2 \boldsymbol{\mu}_0) - |s|^2 \mathbf{s} \cdot \hat{\mathbf{N}} \cdot \mathbf{s} \right) d\mathbf{r}, \quad (\text{S1})$$

where $\boldsymbol{\mu}_0$ is the static magnetization distribution, \hat{N} is the operator of magnetic self-interactions (exchange, dipolar, anisotropy, etc.), and integration goes over the whole sample volume V . Substituting dynamic magnetization \mathbf{s} in the form of the eigenmodes sum $\mathbf{s} = \sum a_i \mathbf{s}_i + \text{c.c.}$, where a_i and \mathbf{s}_i are mode amplitude and profile, respectively, one finds rather cumbersome equations for all four-magnon coefficients.

Yet, such calculations require very pure profiles of spin-wave modes. In our case, the intermode distance is small and resonance peaks overlap significantly (see Fig. 3 in main text). Application of excitation field with specific profile (e.g., uniform, antisymmetric, circular, etc.), does not assist in the excitation of specific modes due to mode hybridization and complex static magnetization distribution, while utilization of drastically decreased damping leads to long simulation time. In addition, Oersted fields of dc current changes the static magnetization distribution and the mode structure to some extent, and rigorous consideration requires calculation of nonlinear coefficients at different dc currents.

For the above-mentioned reasons we made simple estimation of nonlinear coefficients instead of rigorous calculations. In our case of thin dots with perpendicular (or close to perpendicular) static magnetization, only two terms are dominant in the expression for nonlinear four-magnon coefficient:

$$W_{12,34} \approx \frac{\omega_M}{2V} \int \left((\mathbf{s}_1 \cdot \mathbf{s}_3^*) \boldsymbol{\mu}_0 \cdot \hat{N} \cdot [(\mathbf{s}_2 \cdot \mathbf{s}_4^*) \boldsymbol{\mu}_0] + (\mathbf{s}_1 \cdot \mathbf{s}_4^*) \boldsymbol{\mu}_0 \cdot \hat{N} \cdot [(\mathbf{s}_2 \cdot \mathbf{s}_3^*) \boldsymbol{\mu}_0] \right) dr, \quad (\text{S2})$$

with magnetodipolar operator $\hat{N} = \int dr' \hat{G}(\mathbf{r}, \mathbf{r}')$ expressed via magnetostatic Green function \hat{G} . For the perpendicular field we assume uniform static magnetization $\boldsymbol{\mu}_0 = \mathbf{e}_z$ and approximate mode profiles as $\mathbf{s} \sim (\mathbf{e}_x + i\mathbf{e}_y) J_m(k_{nm}r) e^{im\varphi}$ with pinned boundary conditions at the dot edges and proper normalization [3]. Thus, we get values $T_0/2\pi = 48$ GHz, $T_1 \approx T_2 \approx T_{01} \approx 2\pi \times 32$ GHz ($T_i \equiv W_{ii,ii}$, $T_{ij} \equiv W_{ij,ij}$), for the calculation of which full localization of mode 0, 1 (2) in thin (thick) layer was assumed. When the field is weakly tilted, the

considered major contribution changes proportionally to $\cos^2 \theta_M$, where θ_M is the magnetization angle. This difference of about 3 to 5% is neglected. For the coefficient $W_{00,12}$ we assume that interaction takes place in the thin layer only, as modes 0 and 1 are mostly localized there. Then, this coefficient is proportional to the part of the dynamic magnetic moment of mode 2 in thin layer, and we get $W_{00,12}/2\pi = 4$ GHz for $\theta_H = 0^\circ$ and $W_{00,12}/2\pi = 13$ GHz in the tilted state. Contribution of interlayer magnetodipolar interaction is much smaller than one within the thin layer, and is neglected.

Nonlinear terms of spin-transfer torque (STT) were calculated as follows. For spatially uniform precession STT term is equal to $\sigma I(1 - |a|^2)a$ [4]. Corresponding nonlinear term in energy is, thus, proportional to $|a|^4$. For spatially nonuniform dynamics we substitute a with a sum of spin-wave modes and averaging over the layer volume. Thus, we find the STT term equal to $\sigma_i I \left(1 - \tilde{\xi}_i |a_i|^2 - 2 \sum_{j \neq i} \tilde{\xi}_{ij} |a_j|^2 \right)$, where nonlinear coefficients are defined as

$$\tilde{\xi}_{ij} = \frac{\langle J_{m_i}^2(k_i r) J_{m_j}^2(k_j r) \rangle}{\langle J_{m_i}^2(k_i r) \rangle \langle J_{m_j}^2(k_j r) \rangle}, \quad (\text{S3})$$

with $\langle f \rangle = (2/R^2) \int_0^R f(r) r dr$ being the spatial averaging. Thus, we get $\tilde{\xi}_0 = 2.1$, $\tilde{\xi}_1 = \xi_2 = 1.55$, $\tilde{\xi}_{01} = 1.43$. Coefficients of nonlinear damping are more phenomenological [4] and cannot be calculated rigorously. For circularly precessing macrospin, the damping is often accounted for as $\tilde{\Gamma} = \Gamma_0(1 + |a|^2)$, i.e., with the same nonlinear term as STT. Thus, we simply assume $\xi = \tilde{\xi}$.

STT efficiency for mode 2, which is different from the ones of modes 0 and 1 due to the localization of this mode in both layers, is calculated in a straightforward manner:

$$\frac{\sigma_2}{\sigma} = \frac{(1 - \beta^2)t_1}{t_1 + \beta^2 t_2}, \quad (\text{S4})$$

where t_1 (t_2) is the thickness of thin (thick) layer and β is the ratio of dynamic magnetization in thick layer to the one in thin layer. Using this expression, we get $\sigma_2 = -0.16\sigma$ for $\theta_H = 0^\circ$ and $\sigma_2 = 0.4\sigma$ for $\theta_H = 2^\circ$.

-
- [1] A. Hamadeh, G. De Loubens, V. Naletov, J. Grollier, C. Ulysse, V. Cros, and O. Klein, *Phys. Rev. B* **85**, 140408 (2012).
 [2] V. V. Naletov, G. De Loubens, G. Albuquerque, S. Borlenghi, V. Cros, G. Faini, J. Grollier, H. Hurdequint, N. Locatelli, B. Pigeau, *et al.*, *Phys. Rev. B* **84**, 224423

- (2011).
 [3] V. Tyberkevych, A. Slavin, P. Artemchuk, and G. Rowlands, "Vector Hamiltonian Formalism for Nonlinear Magnetization Dynamics," (2020), arXiv:2011.13562 [cond-mat.mtrl-sci].
 [4] A. Slavin and V. Tiberkevich, *IEEE Trans. Magn.* **45**, 1875 (2009).